



# Why is Summertime Arctic Sea Ice Drift Speed Projected to Decrease?

Jamie L. Ward<sup>1,2</sup> and Neil F. Tandon<sup>1</sup>

<sup>1</sup>Department of Earth and Space Science and Engineering, York University, Toronto, ON, Canada

<sup>2</sup>Current affiliation: Cooperative Institute for Great Lakes Research, Ann Arbor, MI, USA

**Correspondence:** Neil F. Tandon (tandon@yorku.ca)

**Abstract.** Alongside declining Arctic sea ice cover during the satellite era, there have also been positive trends in sea ice Arctic-average drift speed (AADS) during both winter and summer. This increasing sea ice motion is an important consideration for marine transportation as well as a potential feedback on the rate of sea ice area decline. Earlier studies have shown that nearly all modern global climate models (GCMs) produce positive March (winter) AADS trends for both the historical period and future warming scenarios. However, most GCMs do not produce positive September (summer) AADS trends during the historical period, and nearly all GCMs project decreases in September AADS with future warming. This study seeks to understand the mechanisms driving these projected summertime AADS decreases using output from 17 models participating in the Coupled Model Intercomparison Project phase 6 (CMIP6) along with 10 runs of the Community Earth System Model version 2 Large Ensemble (CESM2-LE). The CESM2-LE analysis reveals that the projected summertime AADS decreases are due to changes in sea surface height (SSH) which act to reduce sea ice motion in the Beaufort Gyre and Transpolar Drift. During March, changes in internal stress and wind stress counteract these tilt force changes and produce positive drift speed trends. The simulated wintertime mechanisms are supported by earlier observational studies, which gives confidence that the mechanisms driving summertime projections are likely also at work in the real world. However, additional research is needed to assess whether the simulated summertime internal stresses are too weak compared to the tilt forces. The projected summertime SSH changes are primarily due to freshening of the Arctic Ocean (i.e. halosteric expansion), with thermal expansion acting as a secondary contribution. The associated ocean circulation changes lead to additional piling up of water in the Russian shelf regions, which further reinforces the SSH increase. CMIP6 models also show evidence of SSH-driven projected decreases in summertime Arctic sea ice motion, but the models show a wide range of regional SSH trend patterns. Due to small ensemble sizes and the unavailability of required daily output, we were not able to further examine mechanisms in the CMIP6 models. Altogether, our results motivate additional studies to understand the role of SSH in driving changes of Arctic sea ice motion.

## 1 Introduction

One of the strongest signals of global climate change is the rapid retreat and thinning of Arctic sea ice, which strongly influences the global energy balance and atmosphere-ocean energy exchange. Long-term sea ice extent (SIE) changes are greatest during the summer melt season (Serreze and Meier, 2019), declining by  $12.7\% \text{ y}^{-1}$  during September 1979-2021, compared to a



25 2.6%  $y^{-1}$  decline during March 1979-2021 (Meier et al., 2022). Record-low SIE has been frequently observed since the mid-  
2010s, with no record recorded during this time period (Parkinson and DiGirolamo, 2021; Meier et al., 2022). Furthermore,  
since 1958, Arctic-average end-of-summer sea ice thickness has declined by 66%, resulting in less multi-year sea ice cover  
(Kwok, 2018) and making existing ice more susceptible to melt. These trends exhibit large spatial variability, with sea ice  
concentration (SIC) decreasing most in the Barents, Kara, and Beaufort Seas (Comiso et al., 2017) and sea ice thickness (SIT)  
30 declining most rapidly in thick, multi-year ice regions in the central Arctic and along the northern coasts of Greenland and  
Canada (Bitz and Roe, 2004; Kwok, 2018).

Accurately simulating historical sea ice conditions using global climate models (GCMs) is crucial for revealing mechanisms  
responsible for sea ice evolution and building confidence in future sea ice projections. GCM performance assessment has been  
greatly facilitated by the successive phases of the Coupled Model Intercomparison Model (CMIP) alongside large ensemble  
35 simulations with particular models like the Community Earth System Model version 1 Large Ensemble (CESM1-LE; Kay  
et al., 2015). Numerous studies comparing Arctic sea ice observations to CMIP and CESM1-LE output indicate that, although  
most GCMs can reproduce sea ice seasonality (e.g., Labe et al., 2018), they struggle to represent average sea ice conditions and  
trends (e.g., Kwok, 2011, 2018; Notz and SIMIP Community, 2020; Keen et al., 2021; Watts et al., 2021). This is especially  
the case for SIT: Only a handful of CMIP3 models reproduce observed winter SIT spatial patterns (Kwok, 2011), and this only  
40 marginally improves for more recent CMIP phases (Stroeve et al., 2012; Watts et al., 2021). Recent model developments, such  
as parameterizing surface melt ponds (Flocco et al., 2012) and adding in “mushy layer” thermodynamics (Bailey et al., 2020)  
to represent sea ice surface properties more comprehensively, produce output that better agrees with sea ice observations (Kay  
et al., 2022). However, given that these state-of-the-art melt pond parameterizations still result in overestimated summer melt  
pond presence (e.g., Webster et al., 2022), and given our evolving understanding of sea ice thermodynamics, further model  
45 improvements are still needed.

In addition to thermodynamic melt and growth, sea ice motion can also induce sea ice change (e.g., Serreze and Meier,  
2019; Wagner et al., 2021). Sea ice moves through the Arctic basin because of winds, ocean currents, ice internal stresses,  
momentum advection, the Coriolis force, and sea surface height (SSH) gradients, which are in turn coupled to SIT and SIC  
(e.g., Hibler, 1979; Connolley et al., 2004; Olason and Notz, 2014; Docquier et al., 2017; Spall, 2019). As ice floes move, they  
50 can diverge from or converge with existing ice (e.g., Kimura et al., 2013) or be exported through Arctic Ocean gates like Fram  
Strait (Kwok et al., 2009; Smedsrud et al., 2017).

The effects of sea ice motion on regional growth and melt processes vary seasonally and depend on existing ice pack  
properties (Chevallier and Salas-Mélia, 2012). In the summer, ice divergence enhances local melt as the low-albedo ocean  
surface absorbs more incoming sunlight. During the cold season when regional surface air temperatures are well below freezing,  
55 sea ice leads allow for energy transfer from the ocean to the atmosphere to promote ice formation (Kimura et al., 2013).  
Converging sea ice enhances SIT, making it more susceptible to thinning (Flato and Hibler III, 1995; Bitz and Roe, 2004)  
but less likely to melt completely by the end of the summer (Chevallier and Salas-Mélia, 2012). In turn, these SIT changes  
influence sea ice deformation (e.g. Docquier et al., 2017) and the roles of wind, ocean, and internal stresses on observed sea  
ice drift (e.g., Steele et al., 1997; Roach and Blanchard-Wrigglesworth, 2022).



60 Arctic sea ice dynamical changes can be characterized in terms of changes in Arctic-average drift speed (AADS). Observed  
AADS has increased over the past 40 years in tandem with sea ice loss, especially in the summer months (Rampal et al., 2009;  
Tandon et al., 2018; Zhang et al., 2022). However, GCMs have varying success in reproducing these trends. Rampal et al.  
(2011) computed annual sea ice drift speed trends using output from CMIP3 models and found that these GCMs significantly  
underestimate observed AADS increase. However, Tandon et al. (2018) found that much of this disagreement stems from  
65 analyzing model and observational data with different temporal resolutions. Nonetheless, CMIP5 models still underestimate  
observed summertime AADS increase over 1979-2014 (Tandon et al., 2018). Tandon et al. (2018) also found a strong sea-  
sonal contrast in projected AADS trends under the Representative Concentration Pathway with 8.5 W m<sup>-2</sup> radiative forcing  
(RCP8.5): March AADS steadily increases until the late 21st century for most CMIP5 GCMs, while September AADS trends  
switch from positive to negative in the early- to mid-21st century. These projected summertime decreases in Arctic sea ice  
70 motion are the focus of this study because they sharply contrast with expectations based on historical trends.

Understanding the mechanisms of these projected summertime trends is an important step toward assessing the realism  
of models and improving confidence in their projections. To this end, we analyze sea ice dynamics-related output from the  
Coupled Model Intercomparison Project phase 6 (CMIP6) with additional in-depth analysis of the Community Earth System  
Model version 2 Large Ensemble (CESM2-LE). This analysis reveals that changes in SSH likely play a central role in driving  
75 these projected decreases in summertime AADS. In section 2, we provide details regarding the model output and our analysis  
methods. In section 3, we discuss CMIP6 and CESM2-LE trends of AADS, and we perform a detailed breakdown of the  
CESM2-LE sea ice momentum budget and SSH changes. Section 4 provides further discussion and concluding remarks.

## 2 Data and Methods

In this study, we examine output from 17 models participating in the Coupled Model Intercomparison Project, Phase 6 (CMIP6)  
80 (Eyring et al., 2016), as listed in Table 1. For all models, we examine Arctic sea ice drift speed and related quantities for March  
(the month of maximum SIE) and September (the month of minimum SIE) over the period 1950-2100. We use the historical  
simulations of CMIP6 for the period 1950-2014 and the Shared Socioeconomic Pathway 585 (SSP585) scenario for the period  
2015-2100. SSP585 is considered a “business-as-usual” scenario with a radiative forcing of 8.5 W m<sup>-2</sup> at the end of the  
21st century, similar to the CMIP5 RCP8.5 scenario (O’Neill et al., 2017), which was analyzed by Tandon et al. (2018).  
85 We analyze only one simulation from each CMIP6 model, using the r1i1p1f1 variant label whenever possible to maintain  
consistent forcing across different models. However, for MIROC6, MIROC-ES2L, CNRM-CM6-1 and CNRM-ESM2-1, the  
r1i1p1f1 variant is not available, and we instead use the r1i1p1f2 variant, which uses an updated version of the external forcing  
(Durack and Taylor, 2022). For CESM2, only the r4i1p1f1 variant was available, which is identical to r1i1p1f1 except for a  
small perturbation applied to the initial state.

90 Following Tandon et al. (2018), we calculate sea ice drift speed from daily output of drift velocity components (CMIP6  
variable names “siu” and “siv”). We choose this time resolution because there is significant submonthly variability in sea ice  
drift direction, and thus calculating drift speed from monthly output of drift components produces highly inaccurate results



**Table 1.** Models and year ranges examined in this study. Except for CESM2-LE, all model simulations were performed as part of CMIP6. See section 3.1 for additional details regarding how the periods of increasing and decreasing September sea ice Arctic-average drift speed (AADS) trends were determined. The information for CESM2-LE is based on the CESM2-LE ensemble average.

Model (Ensemble)	March Years	September Years (Positive AADS Trends)	September Years (Negative AADS Trends)
ACCESS-CM2	1950-2100	1950-2027	2028-2100
AWI-CM-1-1-MR	1950-2100	1950-1992	1993-2100
BCC-CSM2-MR	1950-2100	1950-2006	2007-2100
CESM2 (CMIP6)	1950-2100	1950-2015	2016-2100
CESM2 (CESM2-LE)	1950-2100	1950-2017	2018-2100
CESM2-WACCM	1950-2100	1950-2022	2023-2100
CNRM-CM6-1	1950-2100	1950-2011	2012-2100
CNRM-ESM2-1	1950-2100	1950-2010	2011-2100
EC-Earth3-CC	1950-2093	1950-2014	2015-2067
IPSL-CM6A-LR	1950-2083	1950-2008	2009-2059
MIROC6	1950-2100	1950-2058	2059-2100
MIROC-ES2L	1950-2100	1950-2060	2061-2084
MPI-ESM1-2-HR	1950-2100	1950-2000	2001-2072
MPI-ESM1-2-LR	1950-2100	1950-1987	1988-2074
MRI-ESM2-0	1950-2100	1950-2009	2010-2100
NESM3	1950-2100	1950-2011	2012-2100
NorESM2-LM	1950-2100	1950-2040	2041-2100
NorESM2-MM	1950-2100	1950-2100	–

(Tandon et al., 2018). For computing spatial averages over the Arctic, we use the same domain as used in Tandon et al. (2018): we include all grid points north of 79°N for longitudes 124°W eastward to 103°E, and we include all grid points north of 68°N over all other longitudes. This domain essentially includes all Arctic sea ice except within the Barents and Kara Seas (where there is little to no sea ice cover during September) and the Canadian Arctic Archipelago. Because we wish to focus on drifting (not landfast) sea ice, we also exclude grid points within 150 km of Arctic coastlines, as in previous studies (Rampal et al., 2011; Tandon et al., 2018). We compute the AADS by calculating the drift speed at each latitude-longitude grid point and then taking the area-weighted average over the Arctic domain. (Grid point area has CMIP6 variable name “areacello.”) For the BCC-CSM2-MR and NESM3 models, the areacello variable was not available, and so a latitude-weighted average was performed instead.

In the model output files, drift velocity in regions without sea ice are assigned a special “missing value” that indicates that the data are missing. For calculations of monthly averages, we exclude any days on which sea ice is missing, and we exclude any months for which all values in that month are missing. For trend calculations, we exclude any points where the number



105 of monthly-mean sea ice drift velocity samples is less than five. We have also tested performing trend calculations with a minimum sample size of three months, and our results did not show strong sensitivity to that choice. For all trend calculations (including trends of quantities other than sea ice drift velocity), we mask out regions where sea ice drift velocity trends have not been computed.

Because of the “pole hole” at the North Pole on spherical polar grids, sea ice and ocean models commonly use displaced-pole  
110 and tripolar grids with the pole(s) placed over land. When calculating sea ice drift speed, we use the drift velocity components on the model’s native grid. That is, drift speed equals  $\sqrt{u_n^2 + v_n^2}$ , where  $u_n$  and  $v_n$  are the velocity components on the native grid. However, when examining the velocity components separately, we transform the velocity components to align with the eastward and northward directions using the relationships

$$\begin{aligned}u &= u_n \cos \theta - v_n \sin \theta, \\v &= u_n \sin \theta + v_n \cos \theta,\end{aligned}\tag{1}$$

115 where  $\theta$  is the computed angle between the  $x$  direction on the native grid and the  $x$  (eastward) direction on a spherical polar grid, and  $u$  and  $v$  are the (spherical polar) eastward and northward drift velocity components, respectively. This transformation is applied to the output for all CMIP6 models except BCC-CSM2-1, whose output was already transformed to eastward and northward components (Xiaoyong Yu, personal communication, 2022).

To better understand the dynamical mechanisms responsible for Arctic sea ice drift speed changes, we analyze wind stress,  
120 ocean stress, internal stress and tilt forces. However, the CMIP6 models did not provide output of these quantities at daily resolution, which is needed in order to accurately decompose terms in the momentum budget. For this reason, we also analyze 10 ensemble members of the Community Earth System Model version 2 Large Ensemble (CESM2-LE; Rodgers et al., 2021), which includes all of the daily output needed for our analysis. The CESM2-LE ensemble members were generated through small perturbations to the 1950 initial state. For the 1950-2014 period, CESM2-LE performs the same historical simulation as  
125 in CMIP6. For 2015 onward, CESM2-LE simulates the moderate warming SSP370 scenario instead of the SSP85 scenario we analyze for the CMIP6 models. For all of the CESM2-LE analysis presented in this study, we show ensemble-averaged results unless otherwise stated. The specific output variables used were “siu\_d” and “siv\_d” for the sea ice drift components, “uarea” for grid box area, “strairx\_d” and “strairy\_d” for the wind stress components, “strocnx\_d” and “strocny\_d” for the ocean stress components, and “strintx\_d” and “strinty\_d” for the sea ice internal stress components. We compute the sea surface tilt force  
130 by computing the spatial gradients of the SSH output (variable “SSH\_2”). To obtain the sea ice mass per unit area, we multiply the daily sea ice thickness (variable “sithick\_d”) by the sea ice density ( $917 \text{ kg m}^{-3}$ ), which is constant in CESM2.

### 3 Results

#### 3.1 Arctic sea ice motion trends

Here, we characterize the Arctic-average and regional sea ice drift speed changes in CMIP6 and CESM2-LE output. In Fig. 1,  
135 we show 21-year smoothed AADS calculated from daily velocity components for March and September. (See Methods for



details. For comparison, unsmoothed AADS timeseries are shown in Fig. A1.) As was the case for CMIP5 (Tandon et al., 2018), there is a large (more than a factor of two) intermodel spread in AADS during the historical period. Tandon et al. (2018) argued that, in CMIP5, much of this spread could be explained by choices of prescribed model parameters, such as the air-ice drag coefficient. In CMIP6, March AADS increases over most of the 1950-2100 period (Fig. 1a).

140 During September, AADS trends are positive during most of the 20th century, but then they become negative for all but one model (NorESM2-MM) during the 21st century (Fig. 1c). The periods of increasing and decreasing September AADS trends are also indicated in Table 1. For each model, these periods are determined by first identifying the year during which the 21-year smoothed September AADS reaches a maximum value during the study period. The portion of the study period before and including this year is considered to be the period of positive September AADS trend, and the portion of the study period  
145 after this year is considered to be the period of negative September AADS trend. The year of this AADS trend sign change varies widely among the CMIP6 models, ranging from 1992 for AWI-CM-1-1-MR to 2058 for MIROC6, with a majority of the models (11 out of 17) placing this year during 2000-2030. Tandon et al. (2018) show qualitatively similar results from CMIP5, with increasing March AADS trends over most of 1950-2100, with almost all models producing a switch from positive to negative AADS trends during September.

150 Projected negative September trends in the 21st century vary greatly in magnitude, with some models depicting faster slow-down (e.g., AWI-CM-1-1-MR and CESM2-WACCM) compared to others (e.g., MRI-ESM2.0 and NorESM2-LM). Interestingly, we find that for the IPSL-CM6A and EC-Earth3-CC models, their March AADS decrease and their September AADS increase near the end of the study period. Tandon et al. (2018) also found that some CMIP5 models from other modelling centres exhibit decreasing March AADS in the late 21st century. Buoy observations show increasing AADS trends during both  
155 March and September (Tandon et al., 2018). Thus, the decreases in September AADS projected by nearly all models contrasts dramatically with historical trends and is worthy of further investigation.

In CESM2-LE, March AADS increases almost linearly for the entire time series, starting at  $\sim 8 \text{ km d}^{-1}$  in 1960 and increasing to  $\sim 11 \text{ km d}^{-1}$  by 2090 (Fig. 1b). In contrast, September AADS remains close to  $10 \text{ km d}^{-1}$  between 1960 and 2018 before decreasing to  $5 \text{ km d}^{-1}$  at the end of the study period (Fig. 1d). The CESM2-LE ensemble spread during September  
160 also increases towards the end of the study period. Thus, in agreement with the CMIP6 models, CESM2-LE produces positive March AADS trends over the entire study period (Fig. 1b) and negative September AADS trends over most of the 21st century (Fig. 1d). The negative September trend is especially clear 2025 onward, and much our analysis hereafter will focus on 2025-2100 trends.

Fig. 2 provides more regional detail by showing the March sea ice motion averaged over the end of the historical period  
165 (1991-2010, left column) and the end of the 21st century (2071-2090, right column). During both time periods, there is anti-cyclonic motion in the Beaufort Gyre, and the highest drift speeds are in the eastern Arctic Ocean along the Transpolar Drift (Fig. 2a,b), as found in observations (Kwok, 2011; Howell et al., 2016). Drift speeds are markedly larger in 2071-2090 than in 1991-2010 over the western Arctic, with little to no change in drift speeds along the Transpolar Drift. Thus, much of the simulated increase in March AADS appears to be due to increased drift speed in the Western Arctic. This regional structure

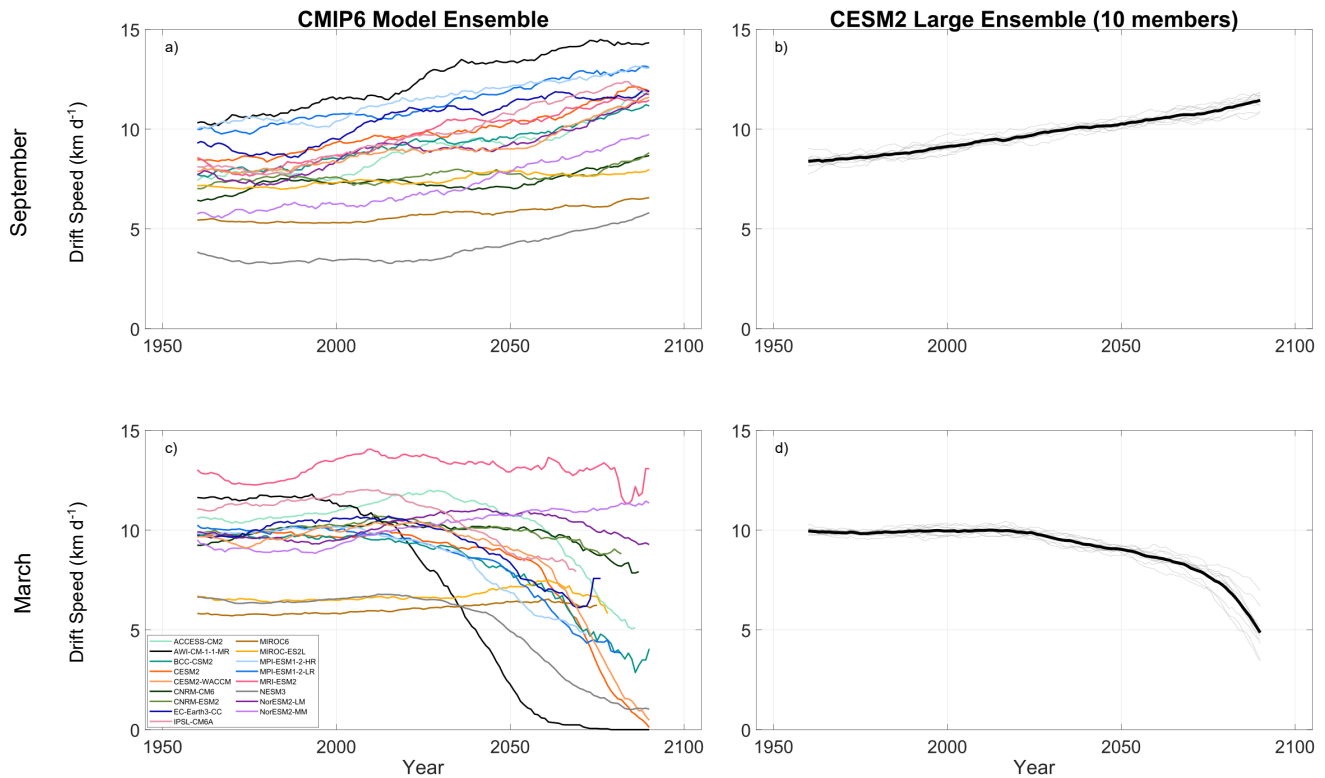


**Figure 1.** AADS simulated in (a,c) CMIP6 and (b,d) CESM2-LE during (a,b) March and (c,d) September. Each timeseries of each CMIP6 model and each CESM2-LE ensemble member is smoothed with a 21-year moving window. In panels b and d, the gray lines indicate individual ensemble members and the thick black lines indicate ensemble averages.

170 is to be expected, since the thickest sea ice is located in the Western Arctic, which means that the greatest declines in sea ice thickness (and thus the greatest drift speed increases) are also in the western Arctic (e.g. Tandon et al., 2018).

175 Comparing the zonal velocity component during the historical and future periods (Fig. 2c,d), we see increasing eastward drift north of Greenland, decreasing westward drift north of the Barents Sea, and increasing westward drift in the Beaufort, Chukchi and East Siberian (BCES) Seas. The meridional velocity component (Fig. 2e) shows northward flow north of Russia and southward flow toward Fram Strait, indicative of the Transpolar Drift crossing the North Pole. There is weak meridional drift in the Beaufort Sea, where drift is mostly in the zonal direction. Comparing the meridional velocity component during the historical and future periods (Fig. 2e,f), we see overall very little change, with a very slight decrease in northward drift north of Russia. There is also a slight decrease in southward drift north of Canada and a slight increase in northward drift off the

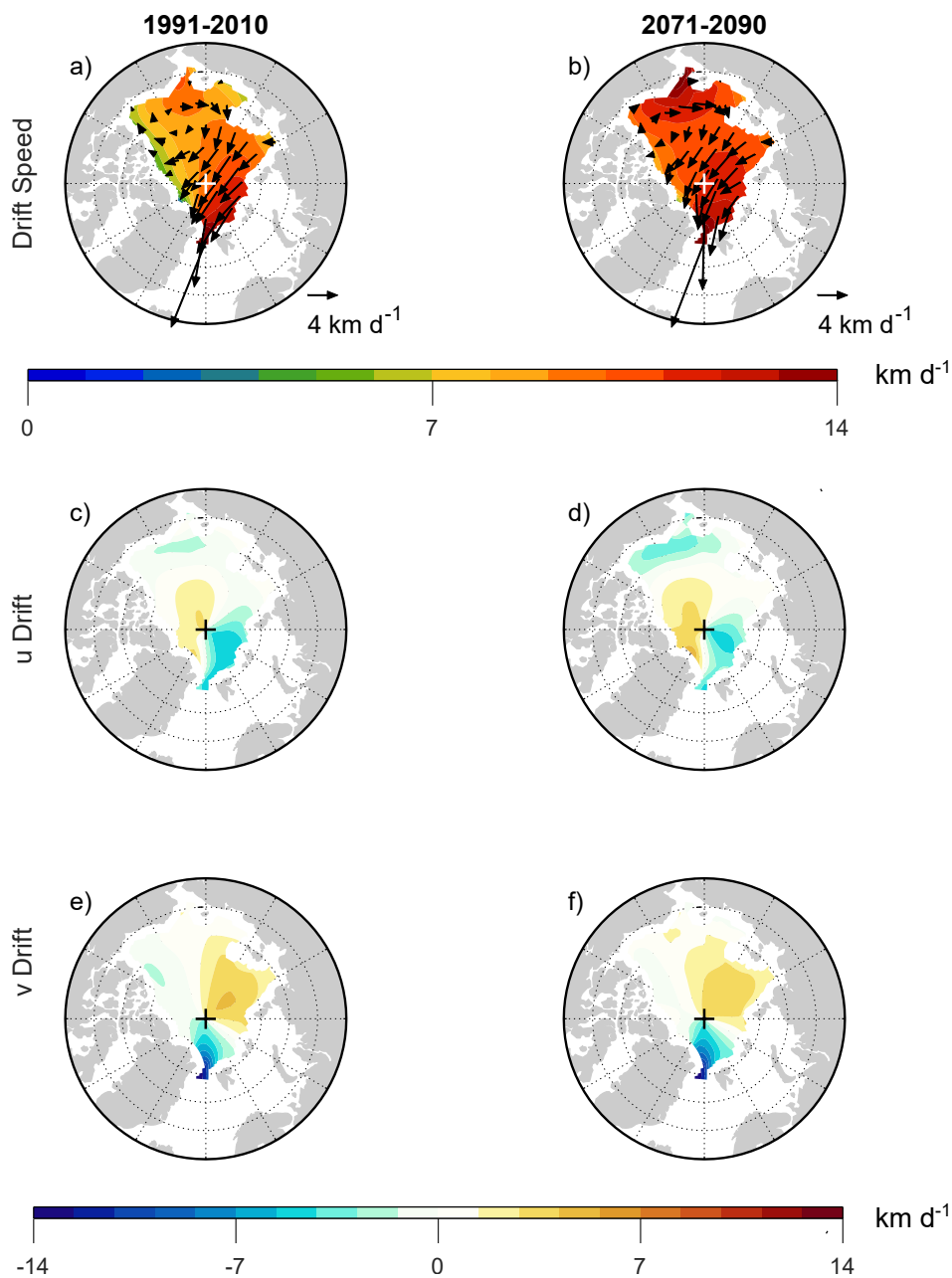


**Figure 2.** CESM2-LE March sea ice (a,b) drift speed magnitude (shading) and drift vectors, (c,d) eastward drift component, and (e,f) northward drift component averaged over (a,c,e) 1991-2010 and (b,d,f) 2071-2090. Note that, because of the nonlinearity in computing drift speed, the shading values in panels (a,b) might differ from the lengths of the overlying vectors in regions where the drift direction is highly variable on submonthly timescales.



Alaskan coast. Altogether, this velocity component analysis indicates that much of the increase in March Arctic-average drift  
180 speed is due to increases in the zonal velocity magnitude in the western Arctic.

In contrast, September drift speeds decrease over most of the Arctic between the historical and future periods (Fig. 3).  
1991-2010 drift speeds range from 8-10 km d<sup>-1</sup>, and the velocity vectors show Transpolar Drift and Beaufort Gyre features  
qualitatively similar to but quantitatively greater than in March (compare Figs. 3a and 2a). The September 2071-2090 average  
depicts lower drift speeds throughout the Arctic, most dramatically in the BCES Seas, where drift speed drops from ~ 7 km d<sup>-1</sup>  
185 to nearly zero (Fig. 3a,b). This decrease combined with weaker decreases elsewhere in the Arctic results in a more spatially  
heterogeneous drift speed field during the future period compared to the historical period. The velocity components reveal that  
much of the speed reduction in the BCES Seas is due to reduced westward drift in these areas (Fig. 3c,d). Previous analysis  
of CMIP6 models indicates that these areas exhibit the earliest transition to seasonal sea ice cover, regardless of the particular  
emission scenario (e.g., Årthun et al., 2021). The more modest decreases in drift speed elsewhere in the Arctic are associated  
190 with a reduction in westward drift north of Canada and in the Transpolar Drift north of Fram Strait (Fig. 3c,d). The latter  
change has also been observed in early 21st century sea ice observations, and it has contributed to a reduction in sea ice  
volume export through Fram Strait (Spreen et al., 2020). Reduced drift speeds also arise from changes in the meridional drift  
component, namely a reduction in northward drift over most of the eastern Arctic and a reduction in southward drift over most  
of the western Arctic (Fig. 3d,e). As was the case in March, however, the largest changes in September drift speed appear to be  
195 associated with changes in the zonal drift component.

The changes highlighted in Figs. 2-3 are also apparent in the projected (2025-2100) regional trends, shown in Fig. 4 shading.  
During March, the strongest trends are positive with overall higher values in the western Arctic than in the eastern Arctic  
(Fig. 4a shading). These trends are associated primarily with increased eastward drift north of Canada and Greenland, accom-  
panied by increased westward drift in the Beaufort Sea (Fig. 4a vectors and Fig. 4c shading). When examining differences  
200 between time periods, there appeared to be an increase in Beaufort Gyre circulation in the Chukchi and East Siberian Seas  
(Fig. 2), but the trends are not westward in these locations (Fig. 4a,c).

The western Arctic also shows positive trends in the meridional drift component (Fig. 4e shading), but this is a region where  
the climatology (contours) is weakly negative. Thus, the positive  $v$  trend here mainly indicates decreasing southward drift, with  
possibly a transition toward slight northward drift, and such a change is not expected to contribute substantially to increased  
205 drift speed. There is also some increasing southward drift near Fram Strait (Fig. 4e), but this is accompanied by decreasing  
westward drift (Fig. 4c), and there is no noticeable effect on drift speed. North of Scandinavia, there is decreasing westward  
drift (Fig. 4c) accompanied by decreasing northward drift (Fig. 4e), contributing to slightly negative drift speed trends here  
(which is not noticeable on the shading scale in Fig. 4a). Altogether, these changes further establish that the positive trend in  
Arctic-average March drift speed is primarily due to increased zonal drift in the western Arctic, which was also apparent in  
210 Fig. 2.

During September, there are negative drift speed trends throughout the Arctic (Fig. 4b), and the changes in drift velocity  
indicate weakening of the Beaufort Gyre and Transpolar Drift (Fig. 4d,f). There is clear weakening of both the zonal and  
meridional velocity components throughout the Arctic. The strongest drift speed trends are in the BCES Seas, which appear

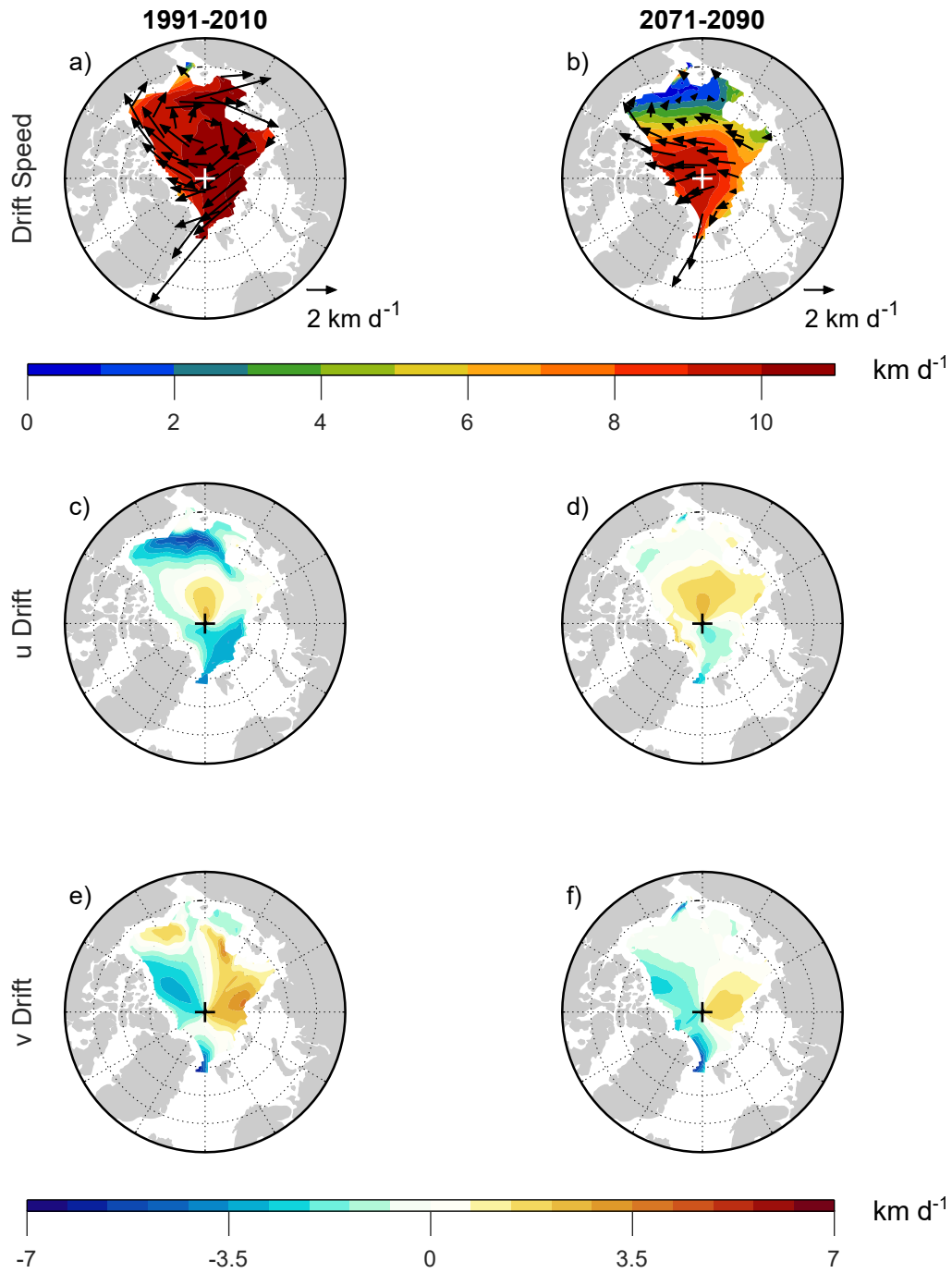


**Figure 3.** As in Fig. 2, but for September. Note that the shading and vector scales are different from those in Fig. 2.

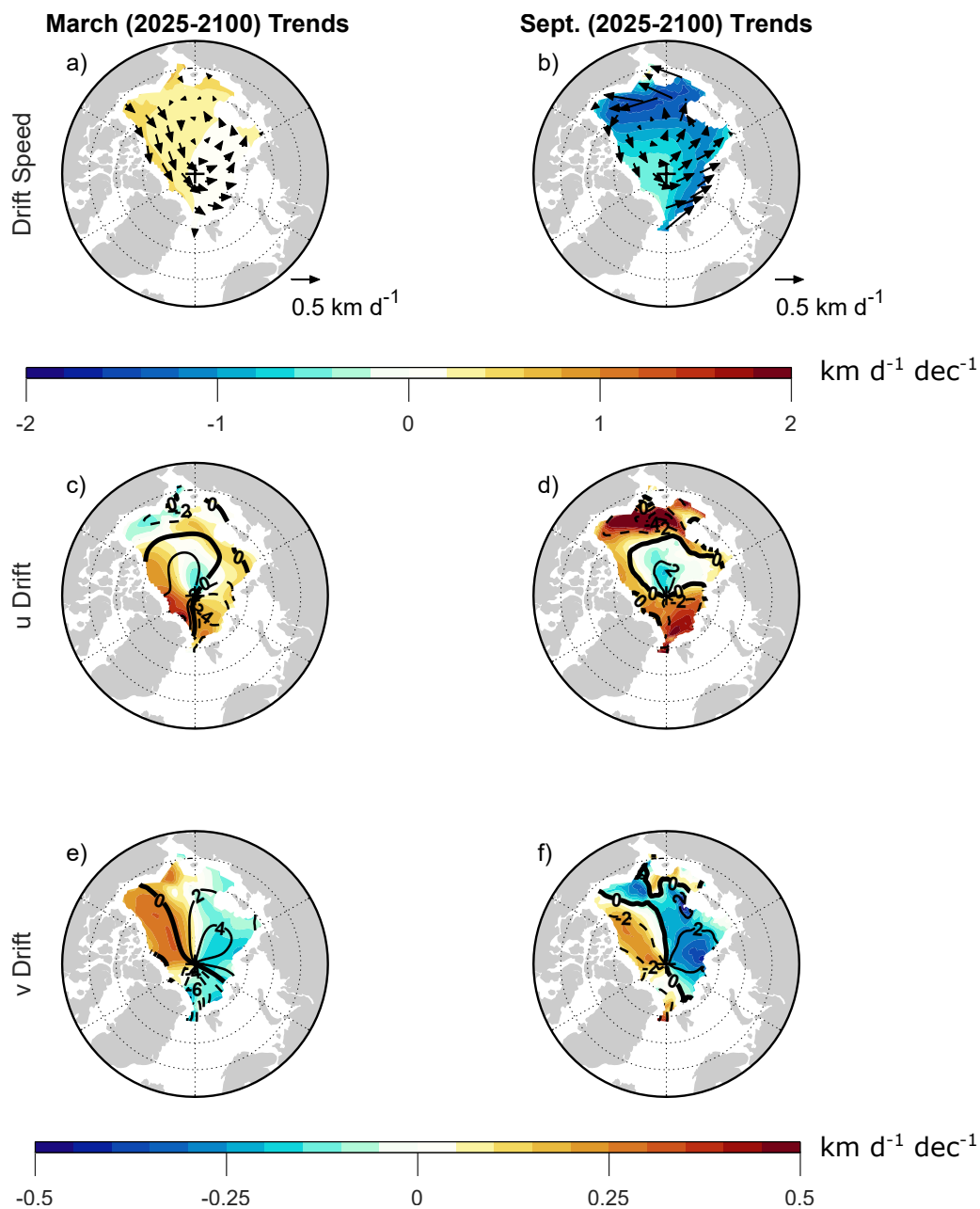


**Figure 4.** Shown in shading are the CESM2-LE trends computed over 2025-2100 for (a,b) sea ice drift speed trends (arrows depict sea ice drift velocity trends), (c,d) the eastward sea ice drift component, and (e,f) the northward component during (a,c,e) March and (b,d,f) September. Contours show climatological values averaged over 2015-2035, with contour interval of  $2 \text{ km d}^{-1}$ . Negative contours are dashed and the zero contours are thick.



to be primarily due to changes in the zonal drift component. These changes further establish that the negative trend in Arctic-  
 215 average September drift speed is primarily due to reduced westward drift in BCES Seas, as was also apparent in Fig. 3,  
 with weakening of northward and westward motion in the Transpolar Drift also an important contribution. Interestingly, there  
 are positive zonal drift trends north of Canada and Greenland, where there are also positive zonal drift trends during March  
 (Fig. 4b,c). However, the climatology of the zonal drift component shows a strong seasonal contrast, with westward drift  
 during September and eastward drift during March. As a result, the positive zonal drift trends act to reduce drift speed during  
 220 September and increase it during March.

### 3.2 Drivers of projected sea ice motion trends

What are the physical mechanisms driving these projected sea ice drift changes? To address this question, we begin with the  
 sea ice momentum equation,

$$\frac{\partial \mathbf{v}}{\partial t} + \mathbf{v} \cdot \nabla \mathbf{v} + \mathbf{f} \times \mathbf{v} = -g \nabla H + \frac{1}{m_A} (\boldsymbol{\tau}_a + \boldsymbol{\tau}_w + \mathbf{F}_i), \quad (2)$$

225 where  $\mathbf{v} = u\mathbf{i} + v\mathbf{j}$  is the drift velocity,  $\mathbf{f} = f\mathbf{k}$  is the Coriolis parameter,  $\boldsymbol{\tau}_a = \tau_{ax}\mathbf{i} + \tau_{ay}\mathbf{j}$  is the wind stress,  $\boldsymbol{\tau}_w = \tau_{wx}\mathbf{i} + \tau_{wy}\mathbf{j}$   
 is the ocean stress,  $\mathbf{F}_i = F_{ix}\mathbf{i} + F_{iy}\mathbf{j}$  is the force due to sea ice internal stress,  $g = 9.8 \text{ m s}^{-2}$  is the gravitational acceleration,  
 $H$  is the SSH, and  $m_A$  is the sea ice mass per unit area (e.g., Hibler, 1979). Since we are interested in long-term averages and  
 trends, we can assume a steady state ( $\partial \mathbf{v} / \partial t = 0$ ). We have also performed analysis verifying that momentum advection [the  
 second term on the left hand side (LHS)] is negligible, as it is two orders of magnitude smaller than other terms. Thus, the  
 230 Coriolis term balances the other forces, and the velocity components are

$$\begin{aligned} u &= -\frac{g}{f} \frac{\partial H}{\partial y} + \frac{1}{fm_A} (\tau_{ay} + \tau_{wy} + F_{iy}), \\ v &= \frac{g}{f} \frac{\partial H}{\partial x} - \frac{1}{fm_A} (\tau_{ax} + \tau_{wx} + F_{ix}), \end{aligned} \quad (3)$$

where subscripts  $x$  and  $y$  denote zonal and meridional components, respectively. To facilitate our discussion, we refer to the  
 SSH-related tilt forces “geostrophic,” and we define the geostrophic velocity components as  $u_g = -\frac{g}{f} \frac{\partial H}{\partial y}$  and  $v_g = \frac{g}{f} \frac{\partial H}{\partial x}$ . We  
 refer to the remaining terms as “ageostrophic,” with components  $u_a = \frac{1}{fm_A} (\tau_{ay} + \tau_{wy} + F_{iy})$  and  $v_a = -\frac{1}{fm_A} (\tau_{ax} + \tau_{wx} + F_{ix})$   
 235 (Armitage et al., 2017). Thus, each velocity component is equal to the sum of its geostrophic and ageostrophic components:  
 $u = u_g + u_a$  and  $v = v_g + v_a$ .

To test our above assumptions, we have computed ensemble mean trends of the force terms on the right hand side (RHS) of  
 (3), and we have compared their sum, which we call the “reconstructed trend,” to the trend of the total velocity field. During  
 March, the total velocity trends and the reconstructed trends are indistinguishable (Figs. 4c,e and A2a,c). During September,  
 240 the total velocity trends and the reconstructed trends are qualitatively similar (Figs. 4d,f and A2b,d), except near Fram Strait,  
 where the reconstructed meridional component trend is opposite in sign to the total meridional component trend (Figs. 4f and  
 A2d). Quantitatively, however, the reconstructed September trends are about 50% smaller than the total velocity trends.

We have found that, even when we attempt to compute the change in velocity between two days from daily fields without  
 neglecting any terms in the momentum equations, there is still quantitative discrepancy with the change in the total velocity



245 field (not shown). Thus, it appears that the quantitative difference between the reconstructed and total September velocity trends is not due to the assumptions made in (3) and is instead due to increased subdaily variability in sea ice motion during September compared to March. This subdaily variability would lead to inaccuracy when attempting to reconstruct velocity from daily output. Numerous earlier studies have shown substantial subdaily variability in Arctic sea ice motion that is present during most months, but nearly disappears during winter freeze-up (Hibler et al., 1974; McPhee, 1978; Colony and Thorndike, 250 1980; Heil and Hibler, 2002). Based on these earlier studies, it is to be expected that our reconstructed trends from daily fields are more quantitatively accurate during March than they are in September. Nonetheless, there is sufficient qualitative accuracy in the reconstructed trends that we use them to decompose contributions to the total drift velocity trends.

As a first step in assessing mechanisms, we examine trends in the geostrophic and ageostrophic velocity components and compare them to the reconstructed trends (Fig. 5). Here, we focus on trends of the zonal drift component, since as shown above, this component captures the key features relevant for trends in Arctic-average drift speed. During March, there is an overall positive trend in  $u_g$ , with peak trends north of Russia and Greenland (Fig. 5c). In contrast, there are negative trends in  $u_a$  throughout the BCES Seas and north of Scandinavia and Russia, with positive trends elsewhere (Fig. 5e). The negative  $u_a$  trend in the BCES Seas is strong enough to produce a negative total  $u$  trend in the Beaufort Sea (Fig. 5a). North of Scandinavia and Russia, the negative  $u_a$  trends act to offset positive  $u_g$  trends, resulting in weakly positive total  $u$  trends here. Positive 260  $u_a$  trends north of Canada and Greenland act to amplify the  $u_g$  trends here, and the strongest total  $u$  trends are in this region. This analysis indicates that March trends are due to a combination of geostrophic (SSH) trends and ageostrophic trends. Both geostrophic and ageostrophic processes substantially contribute to the drift acceleration north of Canada and Greenland, which as noted above, is a key feature responsible for the positive trend in March AADS.

In contrast with the combination of effects during March, September trends are almost completely due to geostrophic changes (Fig. 5b,d,f). Such a contrast is to be expected, as ice is thicker during March, and so ageostrophic forces (such as internal stress) are expected to play a stronger role during March (Sprenn et al., 2011; Docquier et al., 2017). Intriguingly, the geostrophic trends during March and September are nearly identical (Fig. 5c,d). Thus, the contrast between the March and September trends is mainly due to ageostrophic effects during March that are essentially non-existent during September. Overall, these findings contrast with earlier studies showing that ageostrophic terms dominate over geostrophic tilt forces in the sea ice momentum budget (e.g., Steele et al., 1997). Indeed, the dominance of ageostrophic terms is apparent in CESM2-LE's March 2015-2035 270 climatology (compare Figs. 5c and e contours). However, our analysis suggests that such a force balance does not necessarily hold as the sea ice thins and approaches a free drift regime.

What processes are responsible for the ageostrophic velocity trends? To address this question, Fig. 6 shows trends for the internal stress, wind stress and ocean stress terms in the zonal momentum budget. During March, the negative trend in the Beaufort Sea is arising from changes in internal stress (Fig. 6a), whereas the positive trend north of Canada and Greenland is coming primarily from changes in wind stress (Fig. 6c). There is strong cancellation between wind stress and ocean stress trends (Fig. 6c,e), as expected since a change in wind stress is expected to generate an opposing frictional drag by the ocean surface (e.g., Figure 1 of Nakayama et al., 2012). We refer to the combination of wind and ocean stresses as “wind-ocean” stress (Fig. 6g). The wind-ocean stress trend is qualitatively opposite to the internal stress trend (Fig. 6a,g), indicating that

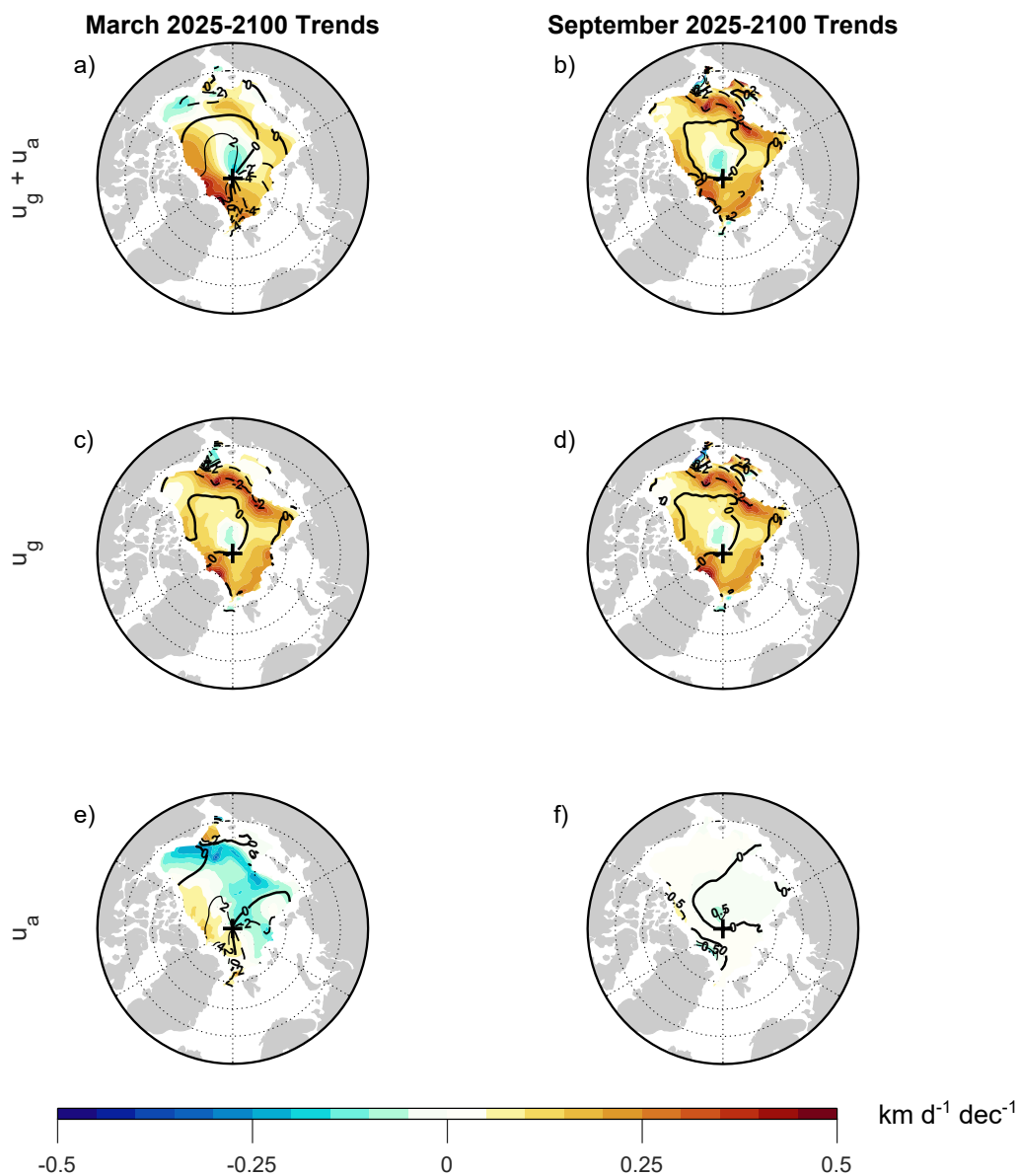


**Figure 5.** Shown in shading are the CESM2-LE trends computed over 2025-2100 for (a,b) the reconstructed zonal drift component, obtained by summing the trends of the geostrophic and ageostrophic terms (see text for details), (c,d) the geostrophic zonal drift component, and (e,f) the ageostrophic zonal drift component during (a,c,e) March and (b,d,f) September. Contours show climatological values averaged over 2015-2035, with contour intervals of (a-e)  $2 \text{ km d}^{-1}$  and (f)  $0.5 \text{ km d}^{-1}$ . Negative contours are dashed and the zero contours are thick. Note that panels a and b are indistinguishable from the sum of the trends of the individual force terms (Fig. A2a,b), which is expected since the trend computation is linear.



280 the internal stress is reacting to the net force exerted by wind-ocean stress as expected. Earlier observational studies have also  
found regional variation in the dominance of internal stress versus wind stress on sea ice motion trends (e.g., Spreen et al.,  
2011), which provides some confidence in the overall realism of the CESM2-LE simulations. However, there is strong internal  
variability influencing the observed trends (Spreen et al., 2011) which confounds a more detailed regional comparison with the  
CESM2-LE trends. During September, there are similarly opposing trends of internal stress and wind-ocean stress (Fig. 6b,h),  
285 but the cancellation appears to be more exact than in March, resulting in near-zero ageostrophic trend. The resulting dominance  
of geostrophic trends motivates further investigation of the processes driving projected SSH changes during September.

### 3.3 Drivers of projected summertime SSH trends

Our earlier analysis motivates further investigation of the projected SSH changes during September. Figure 7a, shading, shows  
that SSH is projected to increase over almost the entire Arctic, with the exception of a slight projected decrease in the central  
290 Arctic. The projected SSH increases are generally higher ( $\sim 3 \text{ cm dec}^{-1}$ ) along the periphery of the basin than over the central  
Arctic. Such a pattern would act to flatten the Arctic “SSH dome” that has been well-documented in observations and models  
(e.g., Koldunov et al., 2014). As we showed earlier, these SSH changes are the primary driver of the September drift velocity  
trends. In particular, Fig. 7a shows that the weakened meridional SSH gradient results in an anomalous cyclonic drift pattern  
(vectors), indicating a slowing down of the Transpolar Drift and the Beaufort Gyre.

295 Following Gill and Niller (1973), the contributions to a change in SSH,  $\eta'$ , can be expressed as

$$\eta' = -\frac{p'_a}{g\rho_0} - \frac{1}{\rho_0} \int_{-H}^0 \rho' dz + \frac{p'_b}{g\rho_0}, \quad (4)$$

where  $p'_a$  is the change in sea level pressure (SLP) exerted by the atmosphere,  $\rho'$  is the change in water density,  $\rho_0 =$   
 $1029 \text{ kg m}^{-3}$  is a reference value for water density,  $p'_b$  is the change in bottom pressure,  $z$  is vertical distance with nega-  
tive values below the mean surface level, and  $H$  is the ocean depth at a given location. The first, second and third terms on the  
300 RHS represent the contributions of surface pressure changes, steric density changes and bottom pressure changes, respectively.  
While the terms in (4) are arranged to solve for SSH change, this expression could also be rearranged into an expression solving  
for bottom pressure, in which case it is equivalent to stating that a change in bottom pressure is determined by the combined  
effects of atmospheric pressure change, SSH change and density change within the ocean column. The only approximation  
entering into this expression is that the contribution of an SSH change to bottom pressure is assumed to be Boussinesq.

305 We now perform calculations from CESM2-LE output to assess each of these contributions. According to (4), if SLP changes  
were the dominant factor, then SLP and SSH changes should be of opposite sign. Indeed, SLP trends are negative over most of  
the Arctic (Fig. 7b), but the peak negative trend lies north of Greenland rather than over the central Arctic. This result suggests  
that SLP trends are likely not the dominant driver of SSH trends. Equation (4) indicates that, if bottom pressure were the  
dominant factor, we would expect SSH and bottom pressure trends to be of the same sign. However, bottom pressure trends  
310 are negative over most of the basin (Fig. 7e), indicating that it cannot be the primary explanation for the positive SSH trends.  
These results suggest that the SSH trends are primarily due to steric changes.

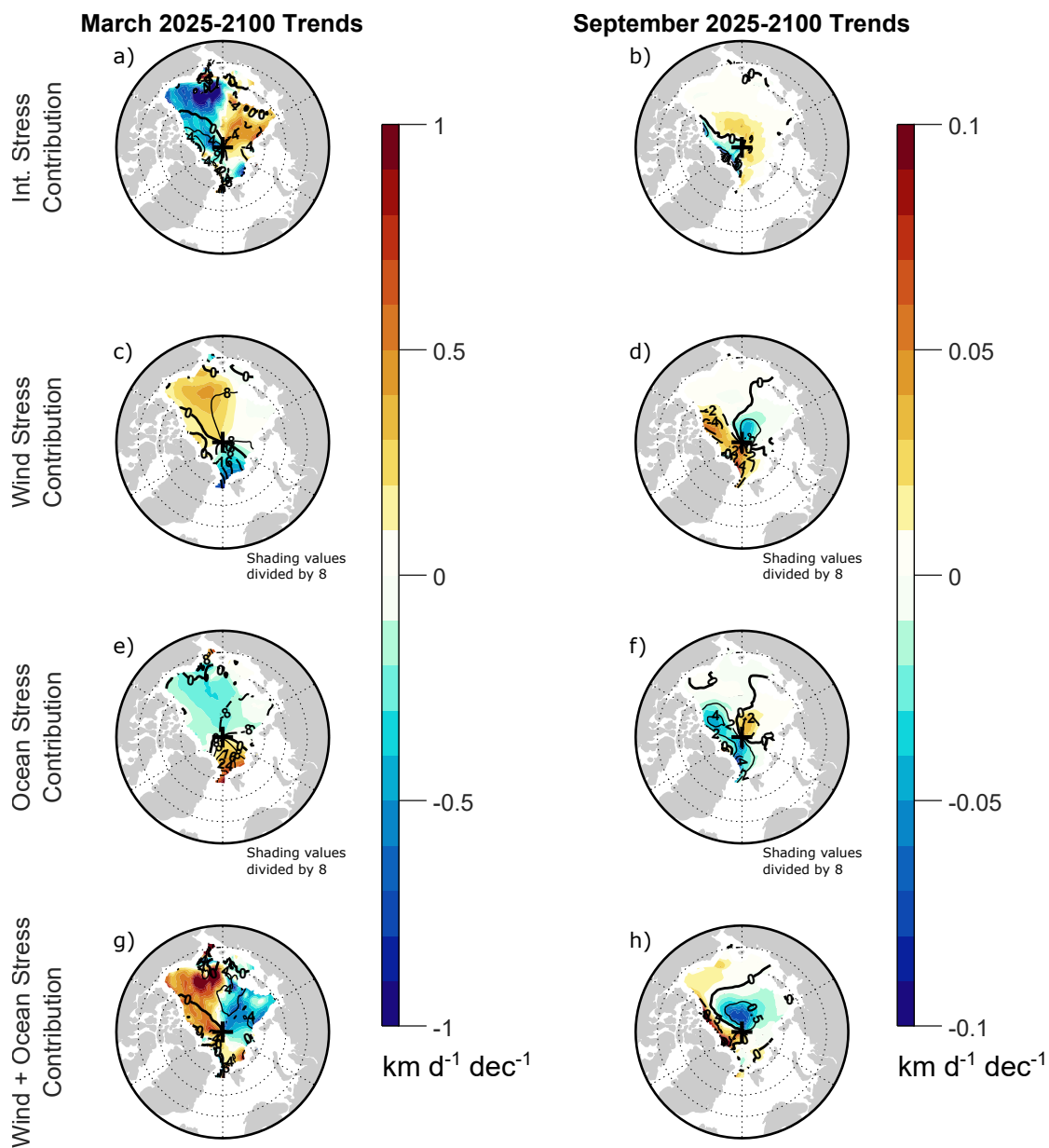


**Figure 6.** Shown in shading are the (a,b) internal stress, (c,d) wind stress, (e,f) ocean stress, and (g,h) wind plus ocean stress contributions to the 2025-2100 trends of the zonal component of sea ice drift velocity in CESM2-LE during (a,c,e,g) March and (b,d,f,h) September. Contours show climatological values averaged over 2015-2035, with contour intervals of (a,g)  $4 \text{ km d}^{-1}$ , (b,h)  $0.5 \text{ km d}^{-1}$ , (c,e)  $8 \text{ km d}^{-1}$ , and (d,f)  $2 \text{ km d}^{-1}$ . Negative contours are dashed and the zero contours are thick. For clarity, the shading values in panels c-f have been divided by eight.

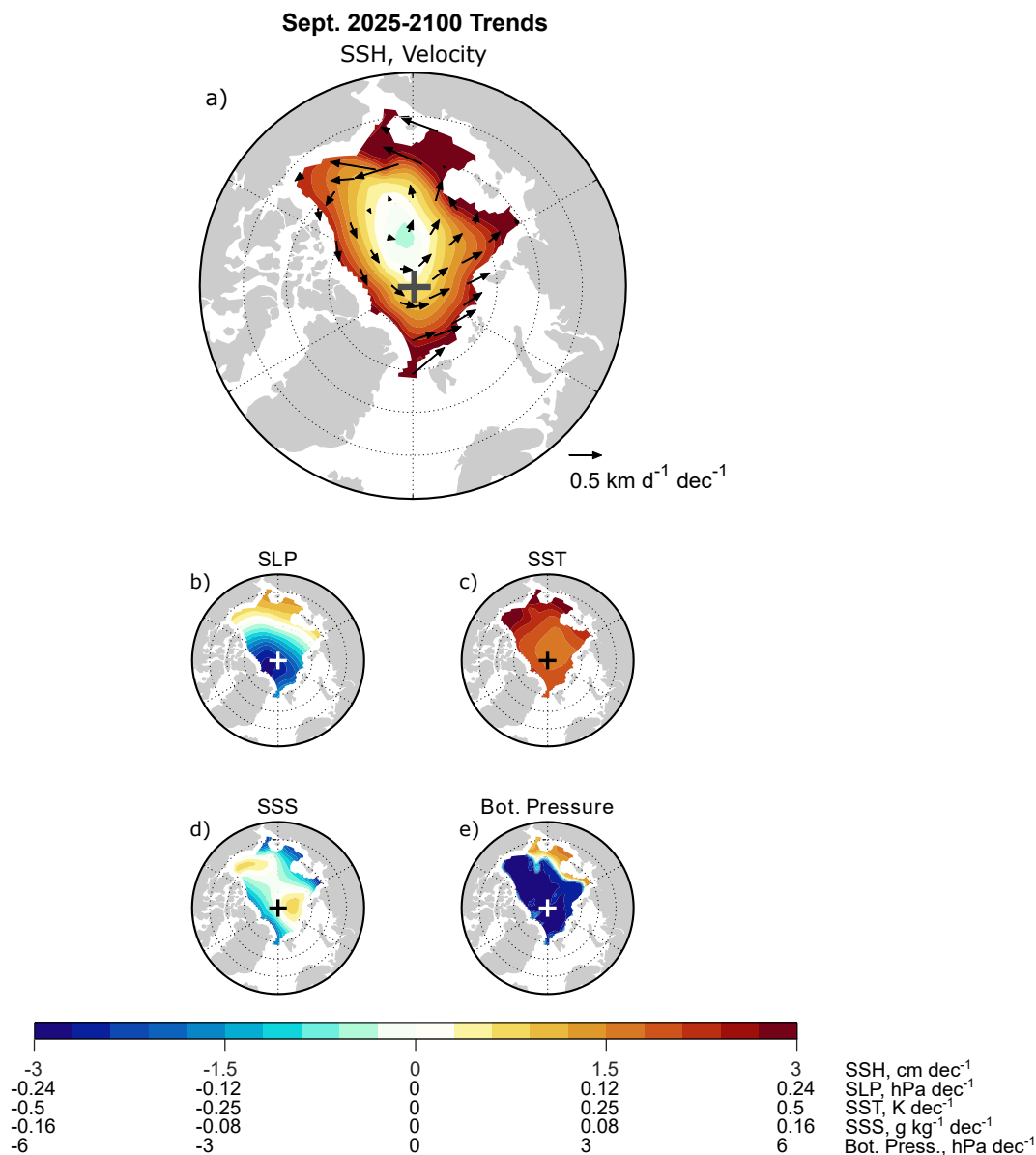


**Figure 7.** CESM2-LE September 2025-2100 trends of (a) SSH (shading) and drift velocity (vectors), (b) sea level pressure, (c) sea surface temperature, (d) sea surface salinity, and (e) ocean bottom pressure.

To get an initial sense of the steric changes, Fig. 7c shows trends of sea surface temperature (SST), which, not surprisingly, is positive over the entire basin. Such warming on its own would be expected to produce decreased density and increased SSH. Sea surface salinity (SSS) trends (Figs. 7d) are negative north of Greenland and Russia, with patterns similar to those found in CMIP5 and CMIP6 models (Wang et al., 2022). These changes would also act to reduce water density and contribute to



increased SSH, while the positive SSS trends elsewhere would act to reduce SSH. These spatially varying SSS trends might be combining with the more spatially uniform SST warming to produce the spatially varying SSH trends. These results provide additional evidence that SSH trends are due to steric changes.

However, to more rigorously attribute thermosteric and halosteric effects, the depth-integrated density (not just surface values) must be considered. To this end, we first define the steric SSH change,  $\eta'_s \equiv -\frac{1}{\rho_0} \int_{-H}^0 \rho' dz$  (i.e. the second term on the RHS of eq. 4). This quantity can then be expanded as

$$\eta'_s = \alpha \int_{-H}^0 T' dz + \beta \int_{-H}^0 S' dz, \quad (5)$$

where  $T'$  is the temperature change,  $\alpha$  is the thermal expansion coefficient,  $S'$  is the salinity change and  $\beta$  is the (negative) saline expansion coefficient (e.g., Gill and Niller, 1973; Rao and Tandon, 2021). On the RHS, the first term represents the thermosteric contribution to SSH change, and the second term represents the halosteric contribution. Although observed  $\alpha$  and  $\beta$  vary by depth (e.g., Fig. 2 in MacIntosh et al., 2017), we have chosen constant values  $\alpha = 7.5 \times 10^{-5} \text{ K}^{-1}$  and  $\beta = -7.6 \times 10^{-4} \text{ kg g}^{-1}$  for all ocean grid points, since specifying  $\alpha$  and  $\beta$  at each level produces nearly identical results (not shown).

Using these values along with the monthly three-dimensional output of ocean salinity and temperature (CESM2 variables “SALT” and “insitu\_temp,” respectively), we have computed halosteric (Fig. 8a) and thermosteric (Fig. 8b) contributions to SSH trends. These results reveal that, while both the halosteric and thermosteric contributions to SSH trends are positive, the halosteric contribution to SSH trends is approximately 50% larger than the thermosteric contribution. This comparison is in agreement with expectations from earlier studies: although thermosteric effects dominate over halosteric effects over most of the global ocean, halosteric effects dominate in the Arctic Ocean because of the near-freezing water temperatures and the relatively low thermal expansion coefficient (Koldunov et al., 2014; Carret et al., 2017). Decadal freshwater variability in the Arctic Ocean has been the greatest contributor to observed SSH change (e.g., Xiao et al., 2020; Lyu et al., 2022), and freshwater changes have been shown to dominate projected SSH changes in CMIP6 under the SSP126 and SSP585 warming scenarios (e.g., Zanowski et al., 2021). In contrast to the contributions implied by SSS changes (Fig. 7d), the depth-integrated halosteric contribution in CESM2-LE is positive over the entire domain (Fig. 8b), suggesting that subsurface freshening of the Arctic Ocean is playing an important role. The analysis of Li and Fedorov (2021) suggests that such freshening is due to advection of salt from the deep Arctic Ocean to lower latitudes in the Atlantic Ocean, and the weakened Atlantic Meridional Overturning Circulation results in greater accumulation of salt at lower latitudes compared to higher latitudes.

Bottom pressure trends are negative over most of the domain (Fig. 8c), with positive trends over the Russian shelf regions. These positive trends appear to be due to anomalous ocean transport toward these shelves (as can be inferred from sea ice drift vector trends in Fig. 7a), which would be expected to pile up water and increase SSH in these areas. Over the interior Arctic basin, however, bottom pressure is more responsive to column-integrated density, which is decreasing. The bottom pressure decreases over the interior Arctic offset some of the steric SSH increase. We have confirmed that the contribution of SLP changes is negligible (Fig. 8d), as it is approximately an order of magnitude smaller than the other contributions. The SSH reconstructed from the sum of the halosteric, thermosteric, bottom pressure, and SLP contributions (Fig. 8e) is very close to the



### Sept. 2025-2100 Trends

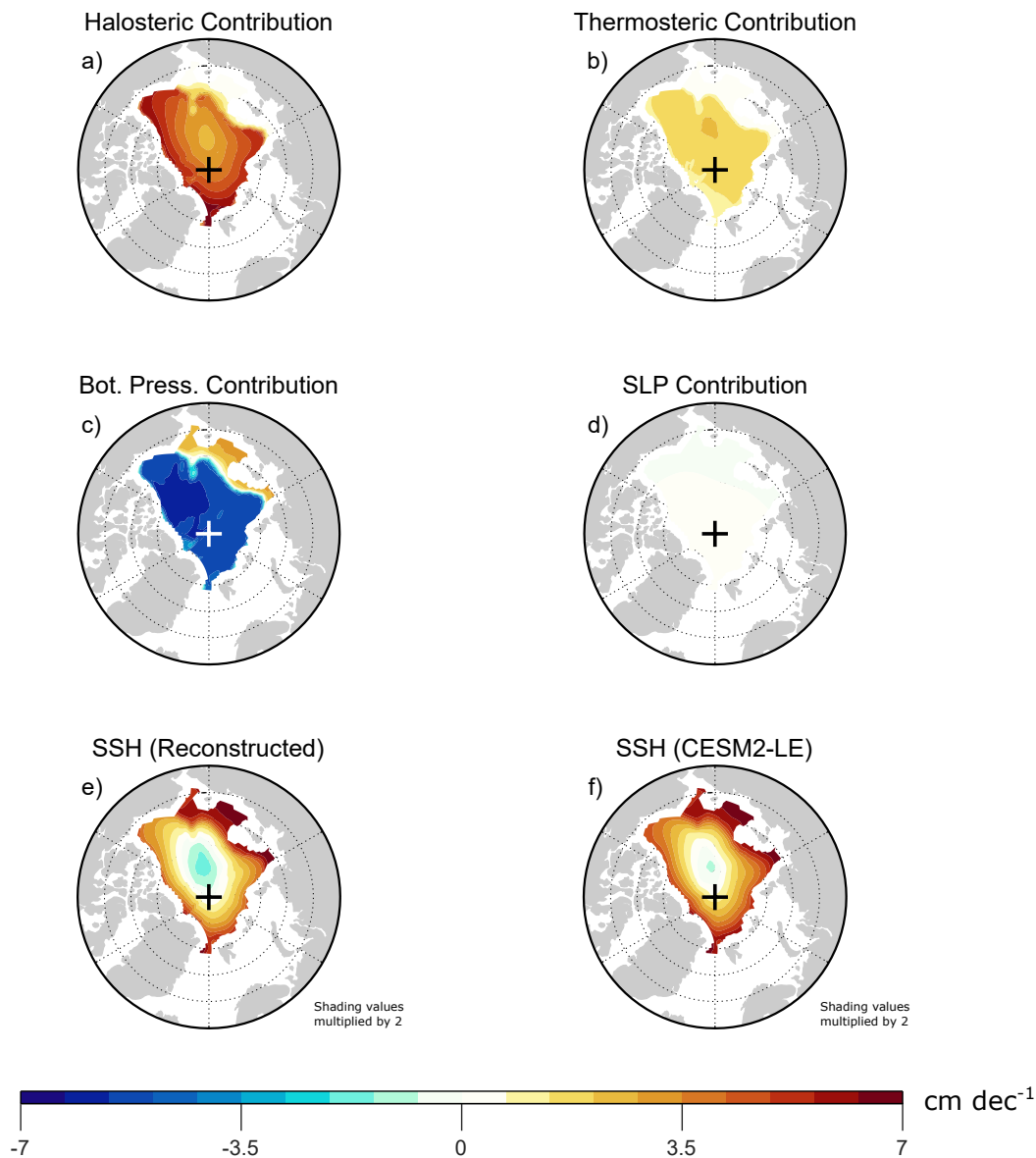


**Figure 8.** CESM2-LE September 2025-2100 trends of (a) the halosteric contribution to SSH, (b) the thermosteric contribution to SSH, (c) the bottom pressure contribution to SSH, (d) the SLP contribution to SSH, (e) SSH reconstructed from the sum of panels a-d, and (f) total SSH directly from CESM2-LE output. Note that, for clarity, the shading scale is different from that used in Fig. 7, and the shading values in panels e and f have been multiplied by two.



SSH trend directly from CESM2-LE output (Fig. 8f), with differences below  $0.5 \text{ cm dec}^{-1}$  that are likely due to our choices  
350 of expansion coefficients. Altogether, our analysis shows that the SSH trend over most of the Arctic is due primarily to salinity  
decreases, enhanced by temperature increases and offset by bottom pressure decreases.

### 3.4 Role of SSH changes in CMIP6 models

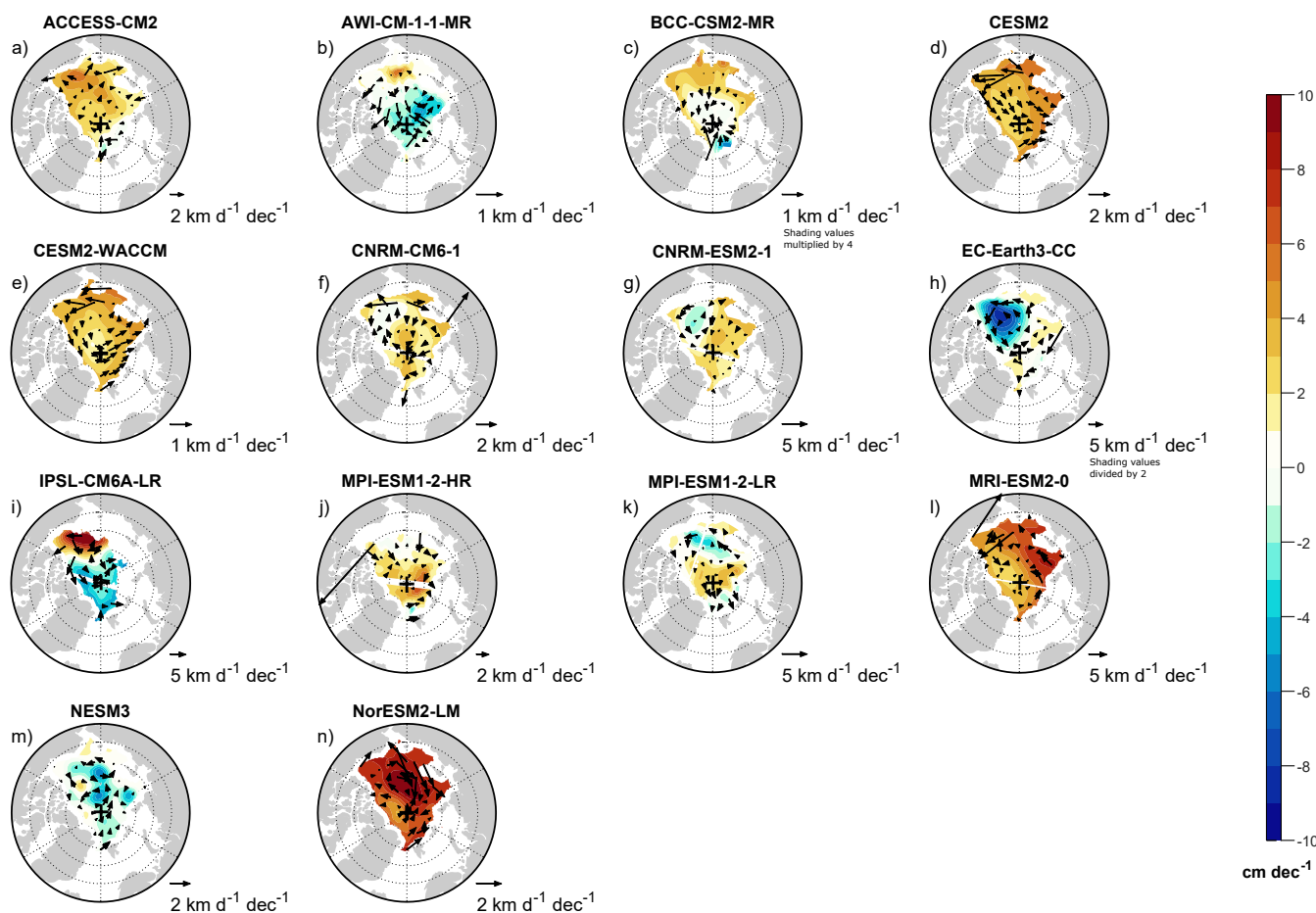
To what extent do CMIP6 models show similar behaviour to CESM2-LE? As stated above, the CMIP6 archive does not include  
the daily fields required for a detailed analysis of the sea ice momentum budget. Nonetheless, we can still compare September  
355 SSH and velocity trends from CMIP6 to get an initial sense for whether SSH changes are driving trends in sea ice motion.

Figure 9 shows projected September SSH trends for 14 models from CMIP6 (shading) with vector drift velocity trends  
overlaid. The models show drift velocity trends that appear to be mostly geostrophic, but with additional spatial variations that  
do not appear to be geostrophic. This increased spatial variation is expected because (in contrast with CESM2-LE) only one  
ensemble member is shown, and thus internal variability has not been filtered out. The role of internal variability is further  
360 substantiated by comparing the single realization trend of CESM2 (Fig. 9d), which shows clear ageostrophic variations, with  
the CESM2-LE trend (Fig. 7a), which is clearly geostrophic. ACCESS-CM2, CNRM-ESM2-1, MPI-ESM1-2-LR, MRI-ESM2-  
0 and CESM2-WACCM show somewhat similar patterns to CESM2-LE in that SSH is projected to increase over most of the  
domain, with greater increases on the basin periphery, resulting in a slowdown of the Transpolar Drift and Beaufort Gyre. AWI-  
CM-1-1-MR, EC-Earth3-CC, IPSL-CM6A-LR and NESM3 also show drift velocity trend patterns associated with a slowdown  
365 of the Transpolar Drift and/or the Beaufort Gyre, but with greater prevalence of negative SSH trends compared to the other  
CMIP6 models mentioned previously. The SSH trend patterns in BCC-CSM2-MR, CNRM-CM6-1, MPI-ESM1-2-HR and  
NorESM2-LM are more spatially complex so that drift speeds up in some regions but slows down elsewhere.

Overall, the CMIP6 results suggest that SSH trends are an important influence on September trends of Arctic sea ice motion.  
However, there is strong variation among models as to the specific patterns of SSH trends, and the reasons for this variation  
370 require further investigation. Some of this variation could simply be due to internal climate variability as mentioned above,  
but much of it could also be due to non-chaotic intermodel differences in physical processes. For example, in some models,  
the halosteric contribution might have more regional variation than in CESM2-LE, or the influence of SLP changes might be  
stronger than in CESM2-LE. Additional work is needed to explore these possibilities, and as with our CESM2-LE analysis,  
such investigation would require consideration of the depth-integrated contributions to SSH changes.

## 375 4 Discussion and conclusion

Our analysis shows that CMIP6 models and CESM2-LE produce AADS trends similar to CMIP5 models (Tandon et al.,  
2018). In climate warming scenarios, the projected AADS trends are generally positive during March and negative during  
September. The negative September trends are of particular interest because they contrast with the positive trends produced by  
buoy observations (Rampal et al., 2009; Tandon et al., 2018).



**Figure 9.** CMIP6 projected September trends of SSH (shading) and sea ice drift velocity (vectors). For the model indicated above each panel, the trend is computed during the period of decreasing September AADS trends (the year ranges indicated in the last column of Table 1), excluding any years before 2025. NorESM2-MM is excluded from this figure because it does not produce negative September AADS trends. MIROC-ES2L and MIROC6 are excluded because the sea ice extent in these models is too low to produce a useful visualization of regional trends. For clarity, the shading values in panel c have been multiplied by four, and the shading values in panel g have been divided by two. The shading scale is different from that used in Fig. 7a.

380 Using daily output from CESM2-LE, we showed that the negative September AADS trends are primarily due to changes in SSH. CESM2-LE projects SSH to increase over most of the Arctic Ocean, with greater increases on the basin periphery. These SSH changes produce geostrophic changes in sea ice drift that act to slow down the Transpolar Drift and Beaufort Gyre. We gained some confidence in the realism of the CESM2-LE simulations because the projected positive trends in March AADS



show contributions from internal stress and wind stress changes that are supported by earlier observational studies (Spren  
385 et al., 2011), although a precise regional comparison is complicated by internal variability in historical trends.

Tandon et al. (2018) also found that, as the Arctic transitioned from complete to partial sea ice cover, simulated sea ice  
drift speed started to decrease, and they referred to this phenomenon as a “sea ice extent effect.” Our analysis reveals that this  
transition arises because, when the sea ice is sufficiently thin, it approaches a free drift state in which tilt forces dominate over  
other forces. This dominance of tilt force contrasts with the force balance for an ice-covered Arctic, in which forces generated  
390 from internal stresses dominate over other forces, causing sea ice to move faster as it thins.

The CESM2-LE September AADS trend during the historical period is essentially flat, which disagrees with the positive  
trend in observations (Tandon et al., 2018). Thus, if CESM2-LE’s SSH mechanism is at work in the real world, it is possible  
that internal stresses are stronger in the real world than they are in CESM2-LE. It is also possible that summertime changes in  
internal stress and wind-ocean stress do not cancel as precisely in the real world as they do in CESM2-LE. Additional work is  
395 needed to compare the balance of these forces in models and observations.

Additional analysis of CESM2-LE output reveals that the positive summertime SSH trends are due primarily to freshening of  
the interior Arctic basin, with warming of the Arctic Ocean acting as a secondary contribution. The corresponding dynamical  
changes also lead to anomalous drift toward the Russian shelf region, resulting in a piling up of water that further reinforces  
the SSH increases.

400 CMIP6 models also show a correspondence between September SSH trends and drift velocity trends, albeit with greater noise  
due to analyzing single ensemble members. The CMIP6 models generally support the notion that SSH changes are playing a  
key role in the sea ice drift velocity changes, but there are also strong contrasts in the projected September SSH trends among  
CMIP6 models. Additional work is needed to understand the extent to which these differences are due to internal climate  
variability or differences in model physics. Such investigations would be greatly facilitated by wider availability of output with  
405 the high temporal resolution necessary for computing terms in the sea ice momentum budget. At minimum, daily temporal  
resolution is required for such analysis, but during summer, subdaily resolution would enable more accurate momentum budget  
decomposition.

*Code and data availability.* CMIP6 data is distributed by the Earth System Grid Federation (ESGF) and can be found at <https://esgf-node.llnl.gov/projects/cmip6/>. CESM2-LE data is maintained by the University Corporation for Atmospheric Research (UCAR) and can  
410 be accessed via <https://www.cesm.ucar.edu/community-projects/lens2/data-sets>. The code used for analyzing these data can be obtained  
from the authors upon request.

## Appendix A

This appendix contains additional figures that support specific points made in the text but are beyond the main focus of this  
study.

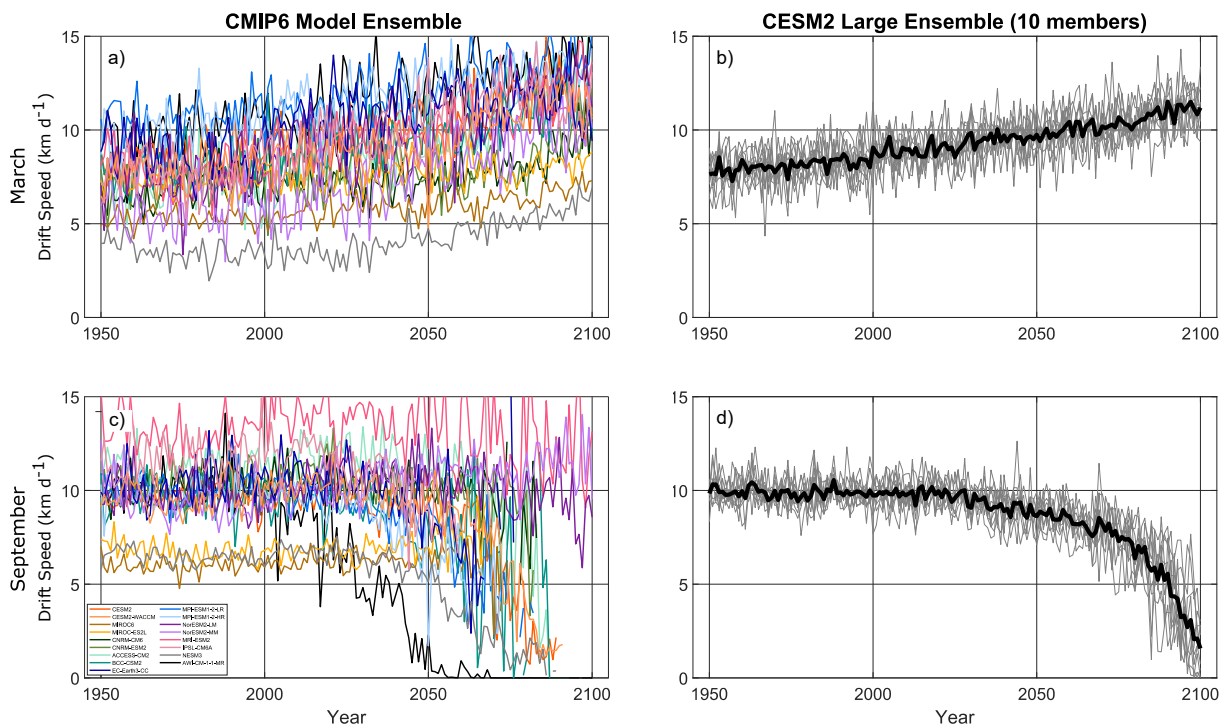


**Figure A1.** As in Fig. 1 but without temporal smoothing applied.

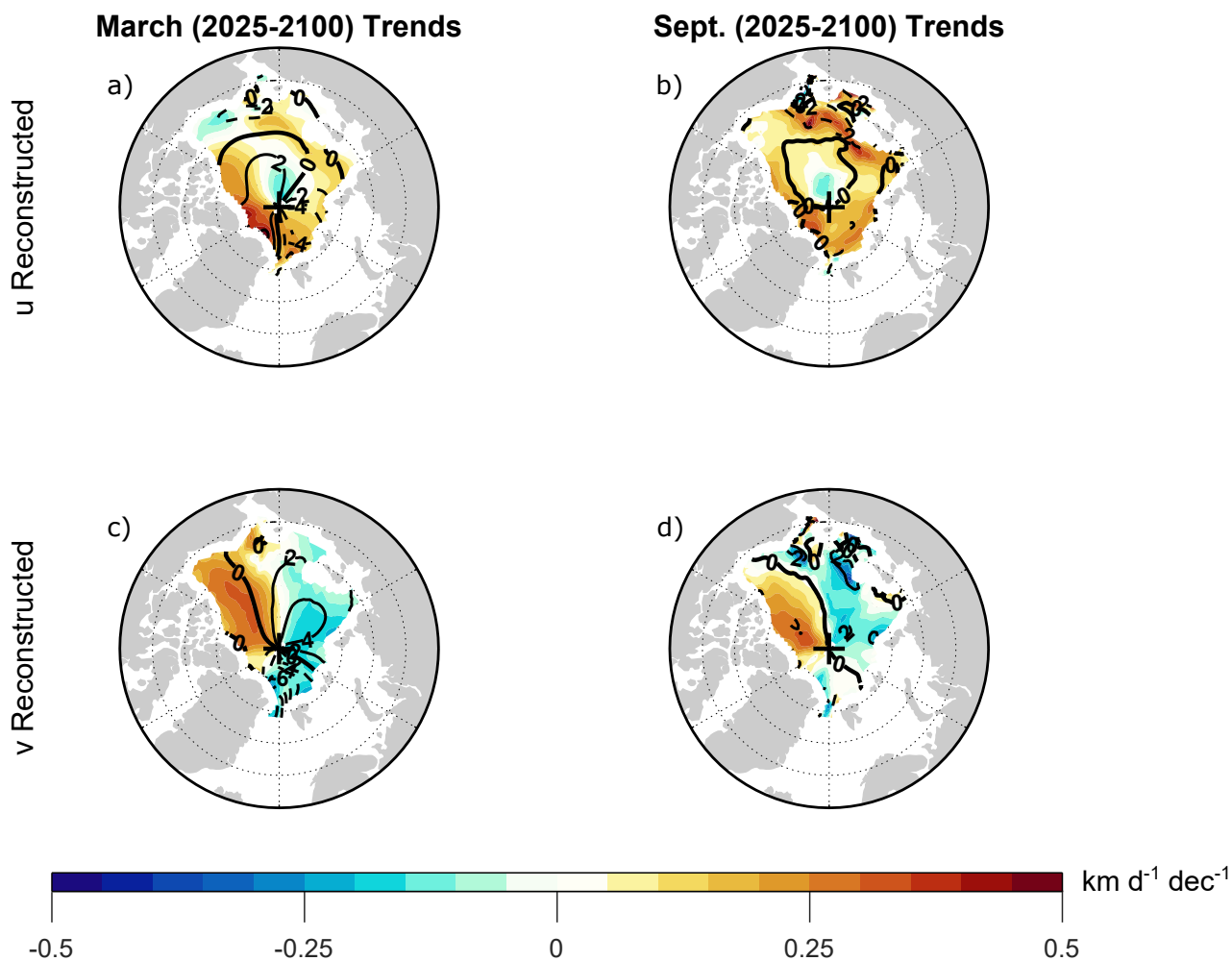


**Figure A2.** Shading shows the CESM2-LE trends obtained by summing the trends of the individual terms on the right hand side of the steady-state (a,b) zonal and (c,d) meridional momentum balance (equation 3) during (a,c) March and (b,d) September 2025-2100. Contours show the climatological reconstructed velocity components averaged over 2015-2035, with contour interval of  $2 \text{ km d}^{-1}$ . Negative contours are dashed and the zero contours are thick.



415 *Author contributions.* JLW acquired the data, analyzed it, created manuscript figures and wrote the manuscript. NFT conceptualized the project, provided guidance for completion and revised the manuscript.

*Competing interests.* The authors declare that they have no competing interests.

*Acknowledgements.* We thank David Docquier and Steve Howell for helpful discussions. We acknowledge the modelling centres that contributed to CMIP6.



## 420 References

- Armitage, T. W., Bacon, S., Ridout, A. L., Petty, A. A., Wolbach, S., and Tsamados, M.: Arctic Ocean surface geostrophic circulation 2003–2014, *The Cryosphere*, 11, 1767–1780, 2017.
- Årthun, M., Onarheim, I. H., Dörr, J., and Eldevik, T.: The seasonal and regional transition to an ice-free Arctic, *Geophysical Research Letters*, 48, e2020GL090825, 2021.
- 425 Bailey, D. A., Holland, M. M., DuVivier, A. K., Hunke, E. C., and Turner, A. K.: Impact of a new sea ice thermodynamic formulation in the CESM2 sea ice component, *Journal of Advances in Modeling Earth Systems*, 12, e2020MS002154, 2020.
- Bitz, C. M. and Roe, G.: A mechanism for the high rate of sea ice thinning in the Arctic Ocean, *Journal of Climate*, 17, 3623–3632, 2004.
- Carret, A., Johannessen, J., Andersen, O. B., Ablain, M., Prandi, P., Blazquez, A., and Cazenave, A.: Arctic sea level during the satellite altimetry era, in: *Integrative Study of the Mean Sea Level and Its Components*, pp. 255–279, Springer, 2017.
- 430 Chevallier, M. and Salas-Mélia, D.: The role of sea ice thickness distribution in the Arctic sea ice potential predictability: A diagnostic approach with a coupled GCM, *Journal of Climate*, 25, 3025–3038, 2012.
- Colony, R. and Thorndike, A.: The horizontal coherency of the motion of summer Arctic sea ice, *Journal of Physical Oceanography*, 10, 1281–1289, 1980.
- Comiso, J. C., Meier, W. N., and Gersten, R.: Variability and trends in the Arctic Sea ice cover: Results from different techniques, *Journal of*
- 435 *Geophysical Research: Oceans*, 122, 6883–6900, 2017.
- Connolley, W., Gregory, J., Hunke, E., and McLaren, A.: On the consistent scaling of terms in the sea-ice dynamics equation, *Journal of Physical Oceanography*, 34, 1776–1780, 2004.
- Docquier, D., Massonnet, F., Barthélemy, A., Tandon, N. F., Lecomte, O., and Fichet, T.: Relationships between Arctic sea ice drift and strength modelled by NEMO-LIM3. 6, *The Cryosphere*, 11, 2829–2846, 2017.
- 440 Durack, P. and Taylor, K.: CMIP6 forcing datasets summary, <http://goo.gl/r8up31>, 2022.
- Eyring, V., Bony, S., Meehl, G. A., Senior, C. A., Stevens, B., Stouffer, R. J., and Taylor, K. E.: Overview of the Coupled Model Intercomparison Project Phase 6 (CMIP6) experimental design and organization, *Geoscientific Model Development*, 9, 1937–1958, 2016.
- Flato, G. M. and Hibler III, W. D.: Ridging and strength in modeling the thickness distribution of Arctic sea ice, *Journal of Geophysical Research: Oceans*, 100, 18611–18626, 1995.
- 445 Flocco, D., Schroeder, D., Feltham, D. L., and Hunke, E. C.: Impact of melt ponds on Arctic sea ice simulations from 1990 to 2007, *Journal of Geophysical Research: Oceans*, 117, 2012.
- Gill, A. and Niller, P.: The theory of the seasonal variability in the ocean, *Deep-Sea Research*, 20, 141–177, [https://doi.org/10.1016/0011-7471\(73\)90049-1](https://doi.org/10.1016/0011-7471(73)90049-1), 1973.
- Heil, P. and Hibler, W. D.: Modeling the High-Frequency Component of Arctic Sea Ice Drift and Deformation, *Journal of Physical Oceanography*, 32, 3039 – 3057, [https://doi.org/https://doi.org/10.1175/1520-0485\(2002\)032<3039:MTHFCO>2.0.CO;2](https://doi.org/https://doi.org/10.1175/1520-0485(2002)032<3039:MTHFCO>2.0.CO;2), 2002.
- 450 Hibler, W. D.: A dynamic thermodynamic sea ice model, *Journal of physical oceanography*, 9, 815–846, 1979.
- Hibler, W. D., Weeks, W. F., Kovacs, A., and Ackley, S. F.: Differential Sea-Ice Drift. I. Spatial and Temporal Variations in Sea-Ice Deformation, *Journal of Glaciology*, 13, 437–455, <https://doi.org/10.3189/S0022143000023212>, 1974.
- Howell, S. E., Brady, M., Derksen, C., and Kelly, R. E.: Recent changes in sea ice area flux through the Beaufort Sea during the summer,
- 455 *Journal of Geophysical Research: Oceans*, 121, 2659–2672, 2016.



- Kay, J. E., Deser, C., Phillips, A., Mai, A., Hannay, C., Strand, G., Arblaster, J. M., Bates, S., Danabasoglu, G., Edwards, J., et al.: The Community Earth System Model (CESM) large ensemble project: A community resource for studying climate change in the presence of internal climate variability, *Bulletin of the American Meteorological Society*, 96, 1333–1349, 2015.
- 460 Kay, J. E., DeRepentigny, P., Holland, M. M., Bailey, D. A., DuVivier, A. K., Blanchard-Wrigglesworth, E., Deser, C., Jahn, A., Singh, H. A., Smith, M. M., et al.: Less surface sea ice melt in the CESM2 improves Arctic sea ice simulation with minimal non-polar climate impacts, *Authorea Preprints*, 2022.
- Keen, A., Blockley, E., Bailey, D. A., Boldingh Debernard, J., Bushuk, M., Delhaye, S., Docquier, D., Feltham, D., Massonnet, F., O'Farrell, S., et al.: An inter-comparison of the mass budget of the Arctic sea ice in CMIP6 models, *The Cryosphere*, 15, 951–982, 2021.
- 465 Kimura, N., Nishimura, A., Tanaka, Y., and Yamaguchi, H.: Influence of winter sea-ice motion on summer ice cover in the Arctic, *Polar Research*, 32, 20 193, 2013.
- Koldunov, N. V., Serra, N., Köhl, A., Stammer, D., Henry, O., Cazenave, A., Prandi, P., Knudsen, P., Andersen, O. B., Gao, Y., et al.: Multimodel simulations of Arctic Ocean sea surface height variability in the period 1970–2009, *Journal of Geophysical Research: Oceans*, 119, 8936–8954, 2014.
- 470 Kwok, R.: Observational assessment of Arctic Ocean sea ice motion, export, and thickness in CMIP3 climate simulations, *Journal of Geophysical Research: Oceans*, 116, 2011.
- Kwok, R.: Arctic sea ice thickness, volume, and multiyear ice coverage: losses and coupled variability (1958–2018), *Environmental Research Letters*, 13, 105 005, 2018.
- Kwok, R., Cunningham, G., Wensnahan, M., Rigor, I., Zwally, H., and Yi, D.: Thinning and volume loss of the Arctic Ocean sea ice cover: 2003–2008, *Journal of Geophysical Research: Oceans*, 114, 2009.
- 475 Labe, Z., Magnusdottir, G., and Stern, H.: Variability of Arctic sea ice thickness using PIOMAS and the CESM large ensemble, *Journal of Climate*, 31, 3233–3247, 2018.
- Li, H. and Fedorov, A. V.: Persistent freshening of the Arctic Ocean and changes in the North Atlantic salinity caused by Arctic sea ice decline, *Climate Dynamics*, 57, 2995–3013, <https://doi.org/10.1007/s00382-021-05850-5>, 2021.
- 480 Lyu, G., Serra, N., Zhou, M., and Stammer, D.: Arctic sea level variability from high-resolution model simulations and implications for the Arctic observing system, *Ocean Science*, 18, 51–66, 2022.
- MacIntosh, C., Merchant, C., and Schuckmann, K. v.: Uncertainties in steric sea level change estimation during the satellite altimeter era: concepts and practices, *Integrative Study of the Mean Sea Level and Its Components*, pp. 61–89, 2017.
- McPhee, M. G.: A simulation of inertial oscillation in drifting pack ice, *Dynamics of Atmospheres and Oceans*, 2, 107–122, [https://doi.org/https://doi.org/10.1016/0377-0265\(78\)90005-2](https://doi.org/https://doi.org/10.1016/0377-0265(78)90005-2), 1978.
- 485 Meier, W., Perovich, D., Farrell, S., Haas, C., Hendricks, S., Petty, A., Webster, M., Divine, D., Gerland, S., Kaleschke, L., Ricker, R., Steer, A., Tian-Kunze, X., Tschudi, M., and Wood, K.: Sea ice [in "State of the Climate in 2021"], *Bull. Amer. Meteor. Soc.*, 103, S270–S273, 2022.
- Nakayama, Y., Ohshima, K. I., and Fukamachi, Y.: Enhancement of Sea Ice Drift due to the Dynamical Interaction between Sea Ice and a Coastal Ocean, *Journal of Physical Oceanography*, 42, 179 – 192, <https://doi.org/https://doi.org/10.1175/JPO-D-11-018.1>, 2012.
- 490 Notz, D. and SIMIP Community: Arctic sea ice in CMIP6, *Geophysical Research Letters*, 47, e2019GL086 749, 2020.
- Olason, E. and Notz, D.: Drivers of variability in Arctic sea-ice drift speed, *Journal of Geophysical Research: Oceans*, 119, 5755–5775, 2014.



- O'Neill, B. C., Kriegler, E., Ebi, K. L., Kemp-Benedict, E., Riahi, K., Rothman, D. S., Van Ruijven, B. J., Van Vuuren, D. P., Birkmann, J., Kok, K., et al.: The roads ahead: Narratives for shared socioeconomic pathways describing world futures in the 21st century, *Global environmental change*, 42, 169–180, 2017.
- 495 Parkinson, C. and DiGirolamo, N.: Sea ice extents continue to set new records: Arctic, Antarctic, and global results, *Remote Sensing and the Environment*, 267, 2021.
- Rampal, P., Weiss, J., and Marsan, D.: Positive trend in the mean speed and deformation rate of Arctic sea ice, 1979–2007, *Journal of Geophysical Research: Oceans*, 114, 2009.
- Rampal, P., Weiss, J., Dubois, C., and Campin, J.-M.: IPCC climate models do not capture Arctic sea ice drift acceleration: Consequences in terms of projected sea ice thinning and decline, *Journal of Geophysical Research: Oceans*, 116, 2011.
- 500 Rao, D. R. and Tandon, N. F.: Mechanism of Interannual Cross-Equatorial Overturning Anomalies in the Pacific Ocean, *Journal of Geophysical Research: Oceans*, 126, e2021JC017 509, 2021.
- Roach, L. and Blanchard-Wrigglesworth, E.: Observed Winds Crucial for September Arctic Sea Ice Loss, *Geophysical Research Letters*, 49, e2022GL097 884, 2022.
- 505 Rodgers, K. B., Lee, S.-S., Rosenbloom, N., Timmermann, A., Danabasoglu, G., Deser, C., Edwards, J., Kim, J.-E., Simpson, I. R., Stein, K., et al.: Ubiquity of human-induced changes in climate variability, *Earth System Dynamics*, 12, 1393–1411, 2021.
- Serreze, M. C. and Meier, W. N.: The Arctic's sea ice cover: trends, variability, predictability, and comparisons to the Antarctic, *Annals of the New York Academy of Sciences*, 1436, 36–53, 2019.
- Smedsrud, L. H., Halvorsen, M. H., Stroeve, J. C., Zhang, R., and Kloster, K.: Fram Strait sea ice export variability and September Arctic sea ice extent over the last 80 years, *The Cryosphere*, 11, 65–79, 2017.
- 510 Spall, M. A.: Dynamics and thermodynamics of the mean transpolar drift and ice thickness in the Arctic Ocean, *Journal of Climate*, 32, 8449–8463, 2019.
- Spreen, G., Kwok, R., and Menemenlis, D.: Trends in Arctic sea ice drift and role of wind forcing: 1992–2009, *Geophysical Research Letters*, 38, 2011.
- 515 Spreen, G., de Steur, L., Divine, D., Gerland, S., Hansen, E., and Kwok, R.: Arctic sea ice volume export through Fram Strait from 1992 to 2014, *Journal of Geophysical Research: Oceans*, 125, e2019JC016 039, 2020.
- Steele, M., Zhang, J., Rothrock, D., and Stern, H.: The force balance of sea ice in a numerical model of the Arctic Ocean, *Journal of Geophysical Research: Oceans*, 102, 21 061–21 079, 1997.
- Stroeve, J. C., Kattsov, V., Barrett, A., Serreze, M., Pavlova, T., Holland, M., and Meier, W. N.: Trends in Arctic sea ice extent from CMIP5, CMIP3 and observations, *Geophysical Research Letters*, 39, 2012.
- 520 Tandon, N. F., Kushner, P. J., Docquier, D., Wettstein, J. J., and Li, C.: Reassessing sea ice drift and its relationship to long-term Arctic sea ice loss in coupled climate models, *Journal of Geophysical Research: Oceans*, 123, 4338–4359, 2018.
- Wagner, T., Eisenman, I., and Mason, H.: How sea ice drift influences sea ice area and volume, *Geophysical Research Letters*, 48, e2021GL093 069, 2021.
- 525 Wang, S., Wang, Q., Wang, M., Lohmann, G., and Qiao, F.: Arctic Ocean freshwater in CMIP6 coupled models, *Earth's Future*, 10, e2022EF002 878, 2022.
- Watts, M., Maslowski, W., Lee, Y. J., Kinney, J. C., and Osinski, R.: A spatial evaluation of Arctic sea ice and regional limitations in CMIP6 historical simulations, *Journal of Climate*, pp. 1–54, 2021.



- Webster, M. A., Holland, M., Wright, N. C., Hendricks, S., Hutter, N., Itkin, P., Light, B., Linhardt, F., Perovich, D. K., Raphael, I. A., et al.:  
530 Spatiotemporal evolution of melt ponds on Arctic sea ice: MOSAiC observations and model results, *Elem Sci Anth*, 10, 000 072, 2022.
- Xiao, K., Chen, M., Wang, Q., Wang, X., and Zhang, W.: Low-frequency sea level variability and impact of recent sea ice decline on the sea  
level trend in the Arctic Ocean from a high-resolution simulation, *Ocean Dynamics*, 70, 787–802, 2020.
- Zanowski, H., Jahn, A., and Holland, M. M.: Arctic Ocean freshwater in CMIP6 ensembles: Declining sea ice, increasing ocean storage and  
export, *Journal of Geophysical Research: Oceans*, 126, e2020JC016 930, 2021.
- 535 Zhang, F., Pang, X., Lei, R., Zhai, M., Zhao, X., and Cai, Q.: Arctic sea ice motion change and response to atmospheric forcing between  
1979 and 2019, *International Journal of Climatology*, 42, 1854–1876, 2022.